

Object-based evaluation of precipitation systems in convection-permitting regional climate simulation over eastern China

Ziyue Guo¹, Jianping Tang², Jie Tang³, Juan Fang⁴, and Wei Luo⁵

¹School of Atmospheric Sciences

²School of Atmospheric Sciences, Nanjing University

³Shanghai Typhoon Institute, China Meteorological Administration, Shanghai, China

⁴Nanjing University

⁵Department of Computer Science and Technology

November 22, 2022

Abstract

Based on the object-based tracking algorithm, the precipitation simulation ability of the convection-permitting (CP) regional climate models (RCMs) is evaluated from the viewpoints of the precipitation systems in this work. The characteristics of precipitation systems over eastern China during 1998-2007 derived from the Weather Research and Forecasting model (WRF) with the horizontal grid spacing of ~ 4 km are compared with CMORPH. On the whole, CP RCMs can capture the average duration and eccentricity of all precipitation systems reasonably. However, precipitation systems tend to be stronger but with smaller coverage area in CP RCMs, which leads to the wet biases and dry biases of accumulated precipitation amount in the longer-duration (≥ 48 hr) and shorter-duration (< 48 hr) systems, respectively. Such deficiencies in accumulated precipitation amount of precipitation systems with various durations can be made up by employing spectral nudging technique in CP RCMs to a certain degree. This work further indicates that, to improve the capability of precipitation simulation in CP RCMs, the relationship between intensity and coverage area of precipitation systems should be described properly in CP RCMs, especially for those with shorter-duration.

Hosted file

essoar.10506032.1.docx available at <https://authorea.com/users/532205/articles/597853-object-based-evaluation-of-precipitation-systems-in-convection-permitting-regional-climate-simulation-over-eastern-china>

1 **Object-based evaluation of precipitation systems in convection-permitting**
2 **regional climate simulation over eastern China**

3

4 Ziyue Guo^{1,2}, Jianping Tang^{1,2}, Jie Tang³, Juan Fang^{1,2}, Wei Luo⁴

5 1. Key Laboratory of Mesoscale Severe Weather/Ministry of Education, Nanjing

6 University, Nanjing, 210023, China

7 2. School of Atmospheric Sciences, Nanjing University, Nanjing, 210023, China

8 3. Shanghai Typhoon Institute, China Meteorological Administration, Shanghai,

9 China

10 4. Department of Computer Science and Technology, Nanjing University, Nanjing,

11 210023, China

12 **Corresponding Author:** Juan Fang, School of Atmospheric Sciences, Nanjing

13 University, 163 Xianlin Road, Nanjing, China. Email: fangjuan@nju.edu.cn

14 **Submitted to:** JGR-Atmospheres

15

16

17

18

19

20

21

22

23 **Key Points:**

24 ● General properties of precipitation systems are analyzed in long-term convection-
25 permitting simulations over eastern China.

26 ● Precipitation systems are substantially too intense but with the limited coverage
27 area in convection-permitting simulations.

28 ● Wet biases and dry biases for shorter-duration and longer-duration systems can be
29 reduced by using spectral nudging at convection-permitting scale.

30

31

32

33

34

35

36

37

38

39

40

41

42

43 **Abstract**

44 Based on the object-based tracking algorithm, the precipitation simulation ability of
45 the convection-permitting (CP) regional climate models (RCMs) is evaluated from the
46 viewpoints of the precipitation systems in this work. The characteristics of
47 precipitation systems over eastern China during 1998-2007 derived from the Weather
48 Research and Forecasting model (WRF) with the horizontal grid spacing of ~ 4 km
49 are compared with CMORPH. On the whole, CP RCMs can capture the average
50 duration and eccentricity of all precipitation systems reasonably. However,
51 precipitation systems tend to be stronger but with smaller coverage area in CP RCMs,
52 which leads to the wet biases and dry biases of accumulated precipitation amount in
53 the longer-duration (≥ 48 hr) and shorter-duration (< 48 hr) systems, respectively.
54 Such deficiencies in accumulated precipitation amount of precipitation systems with
55 various durations can be made up by employing spectral nudging technique in CP
56 RCMs to a certain degree. This work further indicates that, to improve the capability
57 of precipitation simulation in CP RCMs, the relationship between intensity and
58 coverage area of precipitation systems should be described properly in CP RCMs,
59 especially for those with shorter-duration.

60

61

62 **Key words:** Convection-permitting; Regional climate model; Precipitation system; Objected-

63 based algorithm; Spectral nudging

64 **1. Introduction**

65 Precipitation is the most challenging climate variables to regional climate models
66 (RCMs), since it relies on the representation of the interaction of multi-scale
67 processes, which cannot be reasonably resolved due to the coarse horizontal
68 resolution of RCMs (typically with a grid spacing of 10-50 km) (Kendon et al., 2017;
69 Prein et al., 2015; Gutowski et al., 2020). Some studies found that these RCMs tend to
70 underestimate the frequency of dry days but overestimate the frequency of light rain
71 days (Fowler et al., 2007; Boberg et al., 2009). And significant problems remain with
72 sub-daily statistics in RCMs, for instance, the simulated peak occurs too early and
73 with larger amplitude of diurnal cycle than in observation (Brockhaus et al., 2008;
74 Kendon et al., 2012). Many efforts have been made to accurately predict precipitation,
75 one of the most effective method is to improve the horizontal resolution of RCMs,
76 which has been the development trend of RCMs.

77

78 When the resolution of RCMs is increased to convection-permitting (CP) scale, it is
79 possible to switch off the cumulus parameterizations, therefore, CP RCMs are
80 expected to add value than coarser RCMs (Kendon et al., 2012; Prein et al., 2015;
81 Fosseur et al., 2015). Many recent results have shown that the spatial distributions of
82 wet day frequency and intensity (Ban et al. 2014; Guo et al., 2019), the diurnal cycle

83 of precipitation (Fosser et al., 2015; Li et al., 2018; Sun et al., 2016; Guo et al., 2020;
84 Yun et al., 2020) and the duration of extreme hourly precipitation (Kendon et al.,
85 2012; Lind et al., 2016) can be reasonably represented in CP RCMs. In conclusion,
86 these analyses and evaluations are consistently believed that convective precipitation
87 at short temporal and small spatial scales in the CP RCMs provides the significant
88 benefit than in coarse RCMs (Prein et al., 2013, Ban et al., 2014; Fosser et al., 2015).
89 However, these evaluations are primarily based on an Eulerian frame, which is
90 examined at grid cells of the observed and simulated fields, rather than focused on the
91 moving precipitation systems in a Lagrangian frame.

92

93 To examine the properties from the viewpoints of the precipitation systems, we need a
94 nontraditional method to track coherent or contiguous regions of grid cells with
95 characteristic attributes of observation and model results. Object-based algorithm has
96 been widely applied to verify the object such as storms (Chang et al., 2016; 2020),
97 cold cloud (Pempel et al., 2017), mesoscale convective systems (MCS) (Fu et al.,
98 2017; Reinares Martínez and Chaboureau, 2018; Chen et al., 2019; Cheeks et al.,
99 2020), and tropical cyclone (Hagos et al., 2013) in short-term simulations at CP scale.
100 Some new results have been discovered by applying this method to CP RCMs, Wang
101 et al. (2019) showed a good agreement with the observation in term of the convective
102 precipitation intensity and size over U.S, but CP RCMs tend to end the convection too
103 soon. And the translation speed of MCSs are underestimated by CP RCMs (Clark et

104 al. 2014). More importantly, Chang et al. (2020) revealed that the uncertainties of
105 duration and size of precipitation systems are responsible for common wet biases in
106 CP RCMs. Therefore, to better understand the model deficiencies of CP RCMs, we
107 need to complementally evaluate the encompassed full spatial and temporal
108 characteristics of precipitation systems such as duration, size and propagation.

109

110 Although some regional climate simulations at CP scales have been conducted over
111 eastern China, most of the verification methods are over the respective grid points of
112 both observation and CP RCMs, such as they mostly focused on the performance of
113 precipitation amount, frequency and intensity (Xiong and Yan, 2013; Li et al., 2018;
114 Yun et al., 2020; Guo et al., 2020). So far, few studies have focused on the
115 climatological characteristics of precipitation systems in a Lagrangian frame over
116 eastern China and their simulation capabilities in CP RCMs. And the disentangle
117 errors in these properties such as occurrence, duration and spatial coverage would be
118 good to understand the underlying source of model deficiencies, which is of vital
119 importance to the radiative budget, water cycle and water resources management over
120 eastern China.

121

122 These motivate us to employ object-based algorithm in observation and CP RCMs to
123 investigate the characteristics from the perspective of precipitation systems (1998-
124 2007) over eastern China. Moreover, spectral nudging (SN) has been shown as an

125 effective method to improve the precipitation features in the coarse horizontal RCMs
126 (Tang et al., 2017; von Storch et al., 2008). Therefore, we also add an experiment
127 using SN in the CP simulation (CP SN), in contrast with the results of without SN (CP
128 NOSN). In this work, we will assess whether CP RCMs are able to simulate
129 characteristics of trajectory, intensity, coverage area and duration, and evaluate the
130 impact of SN on the simulation of the precipitation systems. By analyzing the
131 characteristics of precipitation systems with various duration, our goal is to provide
132 new perspective for improving the precipitation simulation in CP RCMs.

133

134 **2. Data and Methods**

135 **2.1 Model setup and observational data**

136 The Weather Research and Forecasting (WRF) model Version 3.6.1 (Skamarock et al.,
137 2005) is used to downscale the European Centre for Medium-Range Weather Forecast
138 Interim Reanalysis (Dee et al., 2011) to a CP scale over eastern China. Compared to
139 the CP simulation without SN (CP NOSN), we investigate the impact of SN technique
140 on CP simulation (CP SN), in which the SN technique has been conducted on the
141 horizontal wind fields above the boundary layer. Both the CP NOSN and CP SN are
142 run for continuous 10-year (1998-2007) at a grid spacing of 4 km, and the model
143 domain contains 721×721 points in the horizontal and 35 levels in the vertical. More

144 details on model configuration, such as model spin-up and physical options are
145 consistent with Guo et al. (2020). We compare the model output to the satellite
146 rainfall CMORPH V1.0 dataset (CMORPH for short) (Joyce et al., 2004) with the
147 high spatial resolution of 8 km (at the equator) and 30 min temporal resolution, which
148 has been shown to be suitable for the sub-daily precipitation over eastern China (Chen
149 et al., 2018). The warm-seasons over eastern China are from May to September, and
150 the major rainy seasons are from June to July. Considering the continuity of
151 precipitation systems that are identified and tracked, the MJJASO (May-June-July-
152 August-September-October) season are chosen as validation time period in this work.

153

154 **2.2 Object-based algorithm**

155 Objected-based algorithm is used to identify and track precipitation systems from the
156 hourly dataset for both CMORPH and CP simulations in an identical manner.
157 Precipitation systems are the same as MCSs, they will go through the birth,
158 development and extinction in the temporal scale, and also involve certain impacted
159 areas in the spatial scale. To identify the precipitation systems in spatiotemporal
160 observed and modeled dataset, we firstly utilize the rain-rate threshold to define the
161 rain cells at single time step, and then the area-overlap algorithm is employed to
162 determine trajectories of the rain cells over different time steps, which has been
163 widely used for tracking the MCSs (Cheeks et al., 2020, Fu et al., 2017),

164

165 A precipitation system is defined as a contiguous region with rain-rate larger than 0.1
166 mm/hr and the area greater than minimum rain-area coverage, which is set to 100 grid
167 points (100×8 km×8 km) for CMORPH and 400 grid points (400×4 km×4 km) for
168 CP simulations. For two successive time steps, if a rain cell overlaps itself by more
169 than 40% of its area, then they are considered as the same precipitation system. If
170 more than two precipitation systems merge, the largest overlapped rain cell belongs to
171 this precipitation system, and the smaller is assumed to end. If one precipitation
172 system splits into more than two systems, we also assign the largest rain cells to the
173 precipitation system and initialize the smaller rain cells at this time step. Tracking is
174 performed on successive hourly dataset until the rain cell area no longer meet the 40%
175 overlapping-area criteria. And then, we will analyze the duration of all precipitation
176 systems, and only consider the systems last more than 3 hours in both the observation
177 and model simulation. We remove the precipitation systems with the limited coverage
178 area and very short lifetime, because this type of system contributes the negligible
179 rainfall. Finally, we marked the detect precipitation systems as system_1, system_2,
180 system_3, ..., system_N, N stands for the number of precipitation systems we
181 detected.

182

183 Fig. 1 illustrates the comparison results of precipitation systems identified by our
184 object-based tracking algorithm (d-f) and CMORPH (a-c), taking the identification

185 and tracking of precipitation systems occurred in July 2006 as an example. Both the
186 splitting (happened over Jiangxi and Anhui provinces, shown in Figs. 1b, e) and
187 merging (occurred over Qinghai and Ningxia provinces, shown in Figs. 1c, f) of
188 precipitation systems have been well captured by our algorithm. Calculating through
189 the multiple examples, our algorithm can detect about 90% of the accumulated
190 precipitation amount in CMORPH at each time step, which indicating the
191 accumulated precipitation amount tracked by our algorithm at each time step is
192 comparable to the amount from CMORPH. And the spatial correlation coefficients
193 between accumulated precipitation detected by our algorithm at each time step and the
194 precipitation in CMORPH are greater than 0.95, which further proves that it is
195 feasible and reasonable to use the object-based algorithm for the precipitation systems
196 tracking.

197

198 **2.3 Definition of precipitation systems**

199 We characterize precipitation systems with the following metrics:

200 1) Duration: The period between the ending $[E(k)]$ and beginning $[B(k)]$ of each
201 precipitation event (units: hr), $D(k) = E(k) - B(k) + 1, k = 1, 2, 3, \dots, N$, where k denotes
202 the precipitation system.

203 2) Coverage area: The product of the number of grid points at each time step t
204 (denoted as $g(k, t), k=1, 2, 3 \dots N, t=1, 2, 3, \dots D(k)$) and area of the individual grid
205 cell, that is $s(k, t) = g(k, t) \times 8 \text{ km} \times 8 \text{ km}$ for CMORPH, and
206 $s(k, t) = g(k, t) \times 4 \text{ km} \times 4 \text{ km}$ for CP simulations (units: km^2).

207 3) Intensity: The total rainfall average over all grid points at each time step t
208 (denoted as $\int(k, t), k=1, 2, 3 \dots N, t=1, 2, 3, \dots D(k)$, units: mm/hr).

209 4) Eccentricity: The ratio of minor to major axis lengths of the rain areas at each
210 time steps t (denoted as $\varepsilon(k, t), k=1, 2, 3 \dots N, t=1, 2, 3, \dots D(k)$).

211 Trajectories represent the movement of the center of precipitation systems, and the
212 center is defined as the location of the maximum rainfall in each precipitation system
213 (denoted as $(cen_{lat}(k), cen_{lon}(k), k=1, 2, 3 \dots N)$). The moving speed of the
214 precipitation system is defined as the distance traveled over the lifetime of
215 precipitation system divided by the duration (denoted as $spd(k), k=1, 2, 3 \dots N$).

216 Based on the above definitions, the climatological properties of precipitation systems
217 (e.g. intensity, eccentricity, coverage area) can be characterized as the same dimension
218 with duration. The characteristics of the precipitation systems with various durations
219 is to be presented in section 3.2 and 3.3.

220

221 **3. Results**

222 **3.1 Genesis and movement of precipitation systems**

223 All trajectories of precipitation systems from CMORPH, CP NOSN, CP SN and their
224 differences in tracking density are shown in Fig. 2. Overall, total of 68374 trajectories
225 in MAJJSO 1998-2007 is identified from CMORPH, a large number of samples
226 enable us to perform statistically robust analyses. Fig. 2a shows that precipitation
227 systems with the maximum rainfall of more than 10 mm/hr primarily occur over the
228 ocean and along the coast of eastern China. Compared to CMORPH, less trajectories
229 are identified in both CP NOSN and SN (36980 and 38968 respectively, Table 1),
230 which is related to the underestimations of precipitation frequency in CP RCMs (Guo
231 et al., 2019). One of the reasons might be that the thresholds we used have filtered out
232 some precipitation systems, resulting in the fewer trajectories in CP RCMs. Besides,
233 when we upscale the CP RCMs to the same resolution as the CMORPH, the number
234 of trajectories detected from CP RCMs are increased significantly (53776 and 56253,
235 respectively), which is indicating that the less trajectories in CP RCMs are mainly due
236 to the mismatch with the observed horizontal resolution. Moreover, we note that CP
237 RCMs tend to produce maximal rainfall larger than ~10 mm/hr for all precipitation
238 systems (Figs. 2b-c). From Figs. 2d-e we can see that CP RCMs generally
239 overestimate track density by more than 35% over eastern periphery of Tibetan
240 plateau and Yungui Plateau, but underestimate the track density over most eastern

241 China by up to -40%, which is the same reason that there are less trajectories in CP
242 RCMs. We have to realize that the uncertainties of track density in CP RCMs also
243 may be attributed by the deficiencies of precipitation frequency in CMORPH than in
244 daily precipitation dataset from more than 2400 stations over eastern China (Guo et
245 al., 2019), since it somewhat relies on the rainfall estimation from the IR sensors of
246 geostationary satellite (Joyce et al., 2004).

247

248 To investigate the CP RCMs' ability to simulate the more detail characteristics of
249 these trajectories, we further calculate their orientations, which are computed with the
250 angle relative to the east direction. According to the orientation of trajectories, we
251 category them into four groups: i.e. northeastward ($0^\circ \leq angle < 90^\circ$), northwestward (
252 $90^\circ \leq angle < 180^\circ$), southwestward ($180^\circ \leq angle < 270^\circ$) and southeastward (
253 $270^\circ \leq angle < 360^\circ$). The occurrence frequency of trajectories in four directions from
254 observation and simulations are represented in Table 1. In the CMORPH, the number
255 of eastward trajectories account to 61.1% of total observed trajectories, in which
256 31.8% and 29.3% for northeastward and southeastward, respectively. This feature is
257 consistent with that derived from the Advanced Himawari Imager onboard Himawari-
258 8 in Chen et al. (2019). Both CP NOSN and CP SN can generally describe the
259 proportion of the total number of trajectories in four directions, especially for the

260 eastward trajectories (Table 1). However, due to the less trajectories in CP RCMs,
261 there are some deviations in the genesis frequency simulations of trajectories in four
262 directions. For example, CP RCMs are underestimated the genesis frequency of the
263 westward (including northwestward and southwestward) trajectories, which are
264 mainly generated from India and Indo-China in CMORPH (Figure not shown).

265

266 To clearly see where the precipitation systems originated and the moving
267 characteristics, the simulated spatial distribution of genesis frequency and translation
268 speed of all precipitation systems are compared with the observation (Fig. 3). In the
269 CMORPH, precipitation systems mostly generate from the eastern periphery of
270 Tibetan plateau and the eastern coastal region with the frequency of ~19 times or
271 larger (Fig. 3a). The majority of them move eastwards (Fig. 2a, Table 1) with the
272 speed of ~80 km/hr or faster (Fig. 3d). Over the North China Plain and Yangtze-
273 Huaihe River Valley, the frequency of genesis are less (about ~16 times, Fig. 3a) and
274 translating speed of the precipitation systems are slower (~60 km/hr, Fig. 3d),
275 respectively. It is understandable that the motion of precipitation systems is basically
276 related to the horizontal wind speed in the middle troposphere (Figure not shown). On
277 the whole, CP RCMs are able to capture the observed gradient of genesis frequency
278 and moving speed (Figs. 3b-c, e-f). However, they simulate the less frequent of
279 precipitation systems generate especially from North China Plain, Meiyu Region and
280 Sichuan Basin, which is clearly reflecting the model deficiencies (Figs. 3b-c, e-f).

281 Besides, we surprisingly find that the moving speed of precipitation systems in CP
282 RCMs are slower than that derived from observation, which mainly related to the
283 underestimated motion of steering flow on 500 hPa (Figure not shown). This
284 phenomenon is a little different from the point-to-point matches of model and
285 observation (Guo et al., 2020; Li et al., 2018) and they showed that CP RCMs tend to
286 reproduce the afternoon peaks with earlier shift of 1-2hr than CMORPH (Guo et al.,
287 2020) and rain gauge (Li et al., 2018) over eastern China. By utilizing SN technique
288 in CP RCMs, the simulations of genesis frequency and moving speed over Meiyu
289 Region and Sichuan Basin (Fig. 3c, f) are more consistent with the observation (Fig.
290 3a, d), especially for northeastward systems (Figure not shown), which mainly due to
291 the reasonable mid-troposphere wind field in CP SN (Figure not shown). We further
292 confirmed that the better agreement of CP SN can be partly be explained by the use of
293 SN method to large-scale flow patterns, which is consistent with the simulating results
294 of Tang et al. (2017) at coarser resolution of RCMs.

295

296 **3.2 Statistics of precipitation systems duration**

297 Table 2 summarizes the properties of precipitation systems derived from CMORPH
298 and CP NOSN and SN. Although the number of precipitation systems identified from
299 CP RCMs is fewer than that in CMORPH, the average intensity of precipitation
300 systems simulated by CP RCMs (3.2 mm/hr, +77.8%) is significantly stronger than

301 those in CMORPH (1.8 mm/hr). This is consistent with the previous studies based on
302 the point-to-point validation (Yun et al., 2020; Guo et al., 2020; Li et al., 2018).
303 Comparing to the point-to-point validation, the object-based algorithm enables us to
304 evaluate the ability of CP RCMs in simulating the duration and shape of precipitation
305 systems. From Table 2, we can see that the average duration and eccentricity of
306 precipitation systems can be well simulated in CP NOSN and CP SN, and only
307 increase slightly by about +1.1% (8.9 hr) and +1.2% (0.85) compared with CMORPH
308 (8.8 hr and 0.84). However, the uncertainties of average coverage area in CP NOSN
309 ($23241 km^2$) and CP SN ($22314 km^2$) are obviously decreased by -10.6% and -14.0%,
310 respectively. Compared to CP NOSN, CP SN tends to have a smaller coverage area,
311 which may be due to the constraint of large-scale atmospheric circulations in RCMs
312 on the convective development (Tang et al., 2017; von Storch et al., 2008).

313

314 The characteristics of intensity and coverage area of objects, such as MCSs and
315 storms, are commonly illustrated by their probability and cumulative frequency
316 distributions (PDF, CDF) or the scatterplots in the literature (Davis et al., 2006a, b;
317 Clark et al., 2014; Li et al., 2020; Cheeks et al., 2020; Pempel et al., 2017; Prein et al.,
318 2013). However, to see more clearly the uncertainties of coverage area and intensity
319 in CP RCMs, the density-scatter plots of coverage-area-duration, intensity-duration
320 and eccentricity-duration are shown in Fig. 4. In the CMORPH, the shorter-duration (

321 $>48\text{ hr}$) systems occur frequently, but the coverage area beyond $200 \times 10^3 \text{ km}^2$ are
322 extremely rare (Fig. 4a). In addition, the observed shape of intensity-duration just like
323 skewed distribution (Fig. 4d). These features can be well simulated by CP RCMs, but
324 the simulated density-scatter distributions of coverage-area-duration are excessive
325 concentrated (Figs. 4b-c), and the intensity-duration are more dispersed (Figs. 4e-f).
326 We note that there are significant deviations in the simulations of intensity and
327 coverage area of precipitation systems with shorter-duration. To be more specific, the
328 coverage-area-duration distribution of shorter-duration precipitation systems tend to
329 be less dense in both CP NOSN and SN (Figs. 4b and 4c), which corresponds to the
330 underestimations of coverage area in CP RCMs (Table 2). Figs. 4e-f also show the
331 simulated intensity-duration distribution is wider along the intensity axis than that in
332 CMORPH, especially for the systems shorter-duration. This implies that CP RCMs
333 tend to overestimate the intensity of precipitation systems (Table 2, Fig.7 b).
334 However, Figs. 4h-j indicate that the density-scatter of eccentricity-duration in CP
335 NOSN and CP SN are visually not distinguishable from the CMORPH, indicating that
336 CP RCMs have abilities to reproduce the reasonable spatial distribution accumulated
337 amount of precipitation systems.

338

339 CP RCMs can not only accurately simulate the averaged properties of precipitation
340 systems, but also the dependence of intensity on coverage area, which has been shown
341 more important than the values themselves (Davis et al. 2006b). Figure 5 displays the

342 relationship between mean intensity and mean maximal rainfall and coverage area for
343 all precipitation systems (Figs. 5a, d), shorter-duration precipitation systems (Figs. 5b,
344 e) and longer-duration (≥ 48 hr) precipitation systems (Figs. 5c, f). Due to the frequent
345 occurrence of shorter-duration systems (Fig. 4), there are similar features between the
346 shorter-duration systems (Fig. 5b, e) and all precipitation systems (Fig. 5a, d) in
347 CMORPH. Both the observed intensity and maximal rainfall increase along with the
348 expansion of the precipitation system when the coverage area is within $150 \times 10^3 \text{ km}^2$,
349 and show steady constants afterward (Fig. 5a, b, d and e). But for the longer-duration
350 systems, both the intensity and maximal rainfall are almost constant in CMORPH.
351 These observed features changing with the coverage area for longer-duration systems
352 can be well described by CP RCMs. However, for the shorter-duration systems, the
353 significant decreasing of mean intensity and maximal rainfall in CP RCMs are
354 completely contrary to those in the observation (Fig. 5a, b, d and e), especially for
355 smaller coverage area. And this may be because that CP RCMs tend to reproduce
356 more intense and localized precipitation systems, which is causing the uncertainties of
357 intensity and coverage areas in CP RCMs. Clearly, CP SN shows substantial
358 improvements over CP NOSN, it can reduce the intensity and maximal rainfall biases.

359

360 **3.3 Contribution to precipitation amount**

361 The spatial distribution of the accumulated precipitation amount (APA) of all systems,

362 shorter-duration systems and longer-duration systems are given in Fig. 6, and the
363 spatial correlation coefficients (CORs) and root mean square errors (RMSEs) between
364 simulations and observation are listed in Table 3. The large value of observed APA of
365 all systems mainly appears in the Yangtze-Huaihe River Valley and South China with
366 the magnitude over 9 cm/year (Fig. 6a). For the shorter-duration systems in
367 CMORPH, the APA of shorter-duration systems also occurs at the southeastern
368 periphery of Tibetan plateau and the southern coastal China with maximal amount
369 over 7cm/year (Fig. 6d). But for the longer-duration systems, the observed maximal
370 accumulated amount (over 5cm/year) primarily locates along the southeast coastal
371 areas (Fig. 6g). CP RCMs properly simulate the decline of all systems' APA from
372 southeast to northwest, so that the spatial CORs between CP RCMs and CMORPH
373 are 0.78 and 0.80, respectively (Figs. 6b-c, Table 3). It can be found that both CP
374 NOSN and CP SN underestimate the all APA over Mei-yu Region and Southern
375 China, but they overestimate the APA over the area surrounding Sichuan Basin and
376 Yungui Plateau (Figs. 6b-c). Moreover, it is obvious that CP RCMs have dry biases
377 for shorter-duration precipitation systems, but have wet biases for the longer-duration
378 APA (Figs. 6d-f and Figs. 6g-i), which is partly related to the overestimation of
379 maximal intensity shown in Figs. 2a-c. Comparing to CP NOSN, the encouraging
380 results of shorter-duration, longer-duration systems are seen in the CP SN with the
381 higher CORs and the least RMSEs (Table 3).

382

383 We further divide the shorter-duration and longer-duration precipitation systems into
384 nine classes (A-I) according to their durations (Table 3). From the spatial distributions
385 of APA for the nine-classes (Figure not shown) and the associated statistics listed in
386 Table 3. As we expected, CP RCMs can properly represent the APA of precipitation
387 with duration less than 24 hr (Class A-C) with CORs above 0.72 (Table 3). However,
388 we find that CP RCMs have relatively poor simulation of the precipitation systems
389 lasting from 24 hr to 96 hr (class D-F), which mainly occur over eastern periphery of
390 Tibetan plateau (Figure not shown). Surprisingly, we note that CP RCMs have
391 potential capability to capture the precipitation with duration longer than 120 hours
392 (class H-I) (with CORs above 0.68 and small RMSEs), which also can be seen in
393 Figs. 4 and 5. From the spatial COR and RMSEs of the nine-classes systems, we
394 further confirm that the CP SN achieve notable added value for the precipitation
395 amount than CP NOSN.

396

397 To verify what causes the APA of precipitation systems with different durations in CP
398 RCMs, the statistics of the occurrence frequency, contribution to the total
399 precipitation amount, the average intensity and coverage area for the nine-class
400 precipitation systems (class A-I) are comparatively presented in Fig. 7. Consistent
401 with the results using traditional verification and results shown in Fig. 4, we find that
402 the observed shorter-duration systems occur frequently (98.8%; Fig.7a). However,
403 this type of systems only account for 63.7% of total precipitation amount in

404 CMORPH (Fig. 7b). The longer-duration systems remain certain contributions to total
405 precipitation amount, although they rarely occur (Fig. 7b). From Figs. 7c-d, we can
406 see that the observed average intensity of systems does not vary notably (Fig. 7c)
407 while both the observed coverage area (Fig. 7d) changes significantly as the duration
408 increases, which results in the contributions to total precipitation amount changes
409 with duration (Fig. 7b). But for simulations in CP RCMs, the relationship between the
410 average intensity/coverage area/total precipitation amount and duration are different
411 between CP RCMs and CMORPH (Figs. 7 c-d). It can be found that the
412 underestimations of the contribution of total precipitation amount for the shorter-
413 duration systems (class A-D) are caused by the combination with the consistent
414 occurrence frequency and coverage areas changing. While the overestimations of the
415 contribution of total precipitation amount for the longer-duration systems (E-I) are in
416 line with the changing of intensity in CP RCM.

417

418 More importantly, we note that the contributions to the total precipitation amount for
419 shorter-duration and longer-duration systems in CP NOSN and CP SN are resulting in
420 different reasons. By using SN in CP RCM makes more significant contribution to the
421 total precipitation amount for shorter-duration systems than that in CP NOSN (Fig.
422 7b), which is in line with the different intensity variations shown in CP RCMs (Fig.
423 7c). Therefore, we infer that the different shorter-duration precipitation amount
424 between in CP NOSN and CP SN are caused by the bias of intensity. But the different

425 longer-duration precipitation amount in CP NOSN and CP SN are consistent with
426 their different coverage areas. For example, the class G makes bigger contribution to
427 the total precipitation amount in CP SN than that in CP NOSN, which corresponds to
428 the larger coverage area in CP SN than that in CP NOSN. Such a corresponding
429 relation can also be found in classes E, F, H and I.

430

431 **Summary and Conclusions**

432 Object-based algorithm has been applied to identify and track precipitation systems
433 from both observation and CP RCMs over eastern China during the period 1998-2007.
434 The climatological characteristics of precipitation systems such as genesis frequency,
435 translation speed, duration, coverage area and intensity have been investigated in this
436 work. The evaluation of these properties in CP RCMs complements the previous
437 studies that only considered the spatial dimension alone or focused on the case
438 studies. Furthermore, the improving ability of SN technique of CP RCM is analyzed
439 by comparing without SN. Our findings are summarized below.

440

441 For the genesis frequency and trajectories of precipitation systems, we emphasize the
442 spatial matching between CP RCMs and CMORPH. Although CP RCMs produce less
443 precipitation systems than CMORPH, the genesis locations and propagations of the

444 precipitation systems are properly captured in the CP RCMs. The precipitation
445 systems in CP RCMs are more frequently generated from the eastern periphery of
446 Tibetan plateau and Yungui Plateau. And thus, CP RCMs have more track density
447 over there, which may be responsible for the overestimations of precipitation amount
448 in those regions. Consistent with Clark et al., 2014, the moving velocity of
449 precipitation systems are significant slower in CP RCMs than in observation.
450 However, this phenomenon is different from the results of the traditional point-to-
451 point matching of observations and the CP simulations over eastern China, in which
452 the afternoon diurnal peak of precipitation tend to be earlier in CP RCMs (Li et al.,
453 2018; Guo et al., 2020; Yun et al., 2020). Since deep convective precipitation systems
454 usually occurred in the afternoon over eastern China (Yu et al., 2010), which is
455 indicated that the moving speed of convective precipitation systems in CP RCMs tend
456 to be faster, while the speed of non-convective precipitation systems in CP RCMs
457 tend to be slower. Moreover, we further separate these trajectories into four categories
458 (northeastward, northwestward, southwestward and southeastward), it is found that
459 the simulated occurrence frequency of the precipitation systems in the four groups are
460 closer as observation. However, the moving speed in the four groups are
461 underestimated in CP RCMs, especially for the northeastward and southeastward, and
462 these deficiencies of the moving speed in the four groups can be made up by
463 employing SN method in CP RCMs.

464

465 With regards to the climatological properties of precipitation systems over eastern
466 China, CP RCMs describe the duration and eccentricity of the systems appropriately,
467 while large simulating biases are found in the systems' intensity and coverage area.
468 Compared to CMORPH, the model-simulated density-scatter distributions of
469 coverage-area-duration and the intensity-duration are more concentrated and wider,
470 respectively, which corresponds the underestimation of coverage area and over-
471 prediction of intensity in CP RCMs. The analysis on the relationships between
472 intensity/maximum rainfall and coverage area of the precipitation systems indicates
473 that CP RCMs are able to capture the general functional relationships, especially for
474 the longer-duration systems (≥ 48 hr). However, for both shorter-duration (< 48 hr) and
475 longer-duration systems, the intensity derived from CP RCMs is usually too strong
476 when the systems' coverage area is relatively small. The sensitivity experiment with
477 SN shows that SN technique in CP RCMs can be helpful to reduce the biases in
478 intensity and maximal rainfall of all precipitation systems.

479

480 In terms of the accumulated precipitation amount, CP RCMs can satisfactorily
481 simulate the spatial distribution of total precipitation, however, dry and wet biases in
482 shorter-duration and longer-duration systems have found in CP RCMs, respectively.
483 By employing SN method in CP RCMs will revise these bias and have better
484 performance their spatial distributions due to the less root mean square error and
485 higher spatial correlation coefficient than without SN. The added value of CP SN than

486 CP NOSN is reconfirmed by analyzing the accumulated precipitation amount of nine
487 groups (class A-I), which are classified according to the duration of precipitation
488 systems. Furthermore, the different contributions to total precipitation amount
489 between CP NOSN and SN are revealed, for the longer-duration systems (class E-I),
490 the different contributions between CP SN and CP NOSN are primarily resulted from
491 their differences in coverage area. Nevertheless, for the shorter-duration systems, CP
492 SN contributes more to the total precipitation amount than CP NOSN, which are
493 related to the more intense precipitation in CP SN.

494

495 Overall, the climatology characteristics of precipitation systems over eastern China
496 can be reasonably captured in CP RCMs. However, from the perspective of
497 precipitation systems, the simulated intensity and coverage area in CP RCMs tend to
498 be stronger and smaller, respectively. And wet biases and dry biases for shorter-
499 duration and longer-duration systems have been shown in CP RCMs. These
500 deficiencies of CP RCMs need to be further improved, for example, we could improve
501 the simulations of precipitation systems' intensity and coverage areas since they are
502 virtually important factors for precipitation amount deviations in CP RCMs. More
503 importantly, we need to improve the relationship between intensity and coverage area,
504 especially for the locally isolated precipitation systems with shorter-duration.

505

506 It is worthy of noting that the analyses performed in this work are based on the object-

507 based tracking method. On the whole, the object-based tracking algorithm is an
508 efficient and objective method for tracking precipitation systems. This is why the
509 object-based method is widely used for tracking supercells, mesoscale convective
510 systems, tropical cyclones, heat waves and so on. However, there are some issues
511 about this method that needs to be acknowledged or discussed. Although both the
512 rain-rate threshold and area-threshold may arouse some uncertainties, it doesn't make
513 any difference to our conclusion. For example, too many tests have been performed
514 by increasing the area-threshold from 100-200 grid points ($100 \times 8 \text{ km} \times 8 \text{ km}$ - 200×8
515 $\text{km} \times 8 \text{ km}$) for CMORPH and 400-800 grid points ($400 \times 8 \text{ km} \times 8 \text{ km}$ - $800 \times 8 \text{ km} \times 8$
516 km) for CP simulations, respectively. Albeit the occurrence frequency of precipitation
517 systems will decrease, the overestimations of intensity and underestimations of
518 coverage area are also existed. Moreover, it is noted that this method only can provide
519 the time-domain characteristics of individual systems, but without the spatial
520 distribution of systems. Along with the development of the CP RCMs, the case-based
521 evaluations on the simulations of CP RCMs will be more important in the analysis on
522 the added value of CP RCMs. The more efficient and reasonable object-based
523 tracking will do great help to such investigations.

524

525 **Acknowledgments**

526 National Key Research and Development Program of China (2018YFA0606003) and
527 the National Natural Science Foundation of China (41875124, 41875067) jointly fund
528 this work. The numerical calculations in this paper have been done on the computing
529 facilities in the High Performance Computing Center (HPCC) of Nanjing University.
530 The authors also acknowledge with thanks the ECMWF for providing the ERA-
531 interim reanalysis data as driving fields in the simulations, and NOAA's Climate
532 Precipitation Center (CPC) for providing the CMORPH observational data, which is
533 available at ftp://ftp.cpc.ncep.noaa.gov/precip/CMORPH_V1.0/CRT/ . We declare
534 that we have no conflict of interest.

535

536 **Reference**

- 537 Ban, N., Schmidli, J., & Schär, C. (2014). Evaluation of the convection- resolving regional climate modelling
538 approach in decade- long simulations. *Journal of Geophysical Research: Atmospheres*, 119, 7889–7907.
539 <https://doi.org/10.1002/2014JD021478>.
- 540 Boberg, F., P. Berg, P. Thejll, W.J. Gutowski, and J.H.Christensen, (2009). Improved confidence in climate change
541 projections of precipitation evaluated using daily statistics from the PRUDENCE ensemble. *Climate Dyn.*, 32,
542 1097–1106.
- 543 Brockhaus, P., D. Lu`thi, and C. Scha`r, 2008: Aspects of the diurnal cycle in a regional climate model. *Meteor. Z.*,
544 17, 433–443.
- 545 Chang W, Stein ML, Wang J, Kotamarthi VR, Moyer EJ (2016) Changes in spatiotemporal precipitation patterns in
546 changing climate conditions. *J Clim* 29(23):8355–8376.
- 547 Chang, W., Wang, J., Marohnic, J. et al. Diagnosing added value of convection-permitting regional models using
548 precipitation event identification and tracking. *Clim Dyn* 55, 175–192 (2020). [https://doi.org/10.1007/s00382-018-](https://doi.org/10.1007/s00382-018-4294-0)
549 4294-0.

550 Cheeks, S. M., S. Fueglistaler, and S. T. Garner, 2020: A Satellite-Based Climatology of Central and Southeastern
551 U.S. Mesoscale Convective Systems. *Mon. Wea. Rev.*, 148, 2607–2621, <https://doi.org/10.1175/MWR-D-20->
552 0027.1.

553 Chen G, Lan R, Zeng W, Pan H, Li W (2018) Diurnal variations of rainfall in surface and satellite observations at
554 the monsoon coast (South China). *J Clim* 31(5):1703–1724.

555 Chen, D., Guo, J., Yao, D., Lin, Y., Zhao, C., Min, M., et al. (2019). Mesoscale convective systems in the Asian
556 monsoon region from Advanced Himawari Imager: Algorithms and preliminary results. *Journal of Geophysical*
557 *Research: Atmospheres*, 124, 2210–2234. <https://doi.org/10.1029/2018JD029707>.

558 Clark AJ, Bullock RG, Jensen TL, Xue M, Kong F (2014) Application of object-based time-domain diagnostics for
559 tracking precipitation systems in convection-allowing models. *Weather Forecast* 29(3):517–542.

560 Davis, C., B. Brown, and R. Bullock, 2006a: Object-based verification of precipitation forecasts. Part I:
561 Methodology and application to mesoscale rain areas. *Mon. Wea. Rev.*, 134, 1772–1784,
562 doi:10.1175/MWR3145.1.

563 Davis, C., B. Brown, and R. Bullock, 2006b: Object-based verification of precipitation forecasts. Part II:
564 Application to convective rain systems. *Mon. Wea. Rev.*, 134, 1785–1795, doi:10.1175/MWR3146.1.

565 Dee DP, Uppala SM, Simmons AJ, Berrisford P, Poli P, Kobayashi Set al (2011) The ERA-Interim reanalysis:
566 configuration and performance of the data assimilation system. *Q J R Meteorol Soc* 137(656):553–597.

567 Fosser G, Khodayar S, Berg P (2015). Benefit of convection permitting climate model simulations in the
568 representation of convective precipitation. *Climate Dynamics*, 44(1-2), 45-60.

569 Fowler, H. J., S. Blenkinsop, and A. P. Smith, (2007). Estimating change in extreme European precipitation using a
570 multimodel ensemble. *J. Geophys. Res.*, 112, D18104, doi:10.1029/2007JD008619.

571 Fu, S., J. Sun, Y. Luo, and Y. Zhang, 2017: Formation of Long-Lived Summertime Mesoscale Vortices over
572 Central East China: Semi-Idealized Simulations Based on a 14-Year Vortex Statistic. *J. Atmos. Sci.*, 74, 3955–3979,
573 <https://doi.org/10.1175/JAS-D-16-0328.1>.

574 Guo, Z., Fang, J., Sun, X. et al. Decadal long convection-permitting regional climate simulations over eastern
575 China: evaluation of diurnal cycle of precipitation. *Clim Dyn* 54, 1329–1349 (2020).
576 <https://doi.org/10.1007/s00382-019-05061-z>

577 Guo, Z., Fang, J., Sun, X., Yang, Y., & Tang, J. (2019). Sensitivity of summer precipitation simulation to
578 microphysics parameterization over eastern China: Convection-permitting regional climate simulation. *Journal of*
579 *Geophysical Research: Atmospheres*, 124. <https://doi.org/10.1029/2019JD030295>.

580 Gutowski W J , Ullrich P A , Hall A , et al. The Ongoing Need for High-Resolution Regional Climate Models:
581 Process Understanding and Stakeholder Information[J]. *Bulletin of the American Meteorological Society*, 2020,
582 101(5).

583 Hagos, S., Z. Feng, S. McFarlane, and L. R. Leung, 2013: Environment and the Lifetime of Tropical Deep
584 Convection in a Cloud-Permitting Regional Model Simulation. *J. Atmos. Sci.*, 70, 2409–2425,
585 <https://doi.org/10.1175/JAS-D-12-0260.1>.

586 Joyce, R. J., Janowiak, J. E., Arkin, P. A., & Xie, P. (2004). Cmorph: a method that produces global precipitation
587 estimates from passive microwave and infrared data at high spatial and temporal resolution. *Journal of*
588 *Hydrometeorology*, 5(3), 287-296.

589 Kendon, E. J., Roberts, N. M., Senior, C. A., & Roberts, M. J. (2012). Realism of rainfall in a very high-resolution
590 regional climate model. *Journal of Climate*, 25(17), 5791-5806.

591 Kendon, E. J., Ban, N., Roberts, N. M., Fowler, H. J., Roberts, M. J., Chan, S. C., Evans, J. P., Fosser, G., &
592 Wilkinson, J. M. (2017). Do Convection-Permitting Regional Climate Models Improve Projections of Future
593 Precipitation Change?, *Bulletin of the American Meteorological Society*, 98(1), 79-93. Retrieved Jan 21, 2021,

594 from <https://journals.ametsoc.org/view/journals/bams/98/1/bams-d-15-0004.1.xml>

595 Li, P., Furtado, K., Zhou, T., Chen, H., Li, J., Guo, Z., & Xiao, C. (2018) The diurnal cycle of East Asian summer
596 monsoon precipitation simulated by the Met Office Unified Model at convection-permitting scales. *Climate*
597 *Dynamics*, 1-21.

598 Li, Z., Y. Luo, Y. Du, and J. C. L. Chan, 2020: Statistical characteristics of pre-summer rainfall over South China
599 and associated synoptic conditions. *J. Meteor. Soc. Japan*, 98, 213–233, doi:10.2151/jmsj.2020-012.

600 Lind, P., Lindstedt, D., Kjellström, E., & Jones, C. (2016). Spatial and temporal characteristics of summer
601 precipitation over central Europe in a suite of high-resolution climate models. *Journal of Climate*, 29(10), 3501-
602 3518.

603 Prein A F, Langhans W, Fosser G, et al. (2015). A review on regional convection-permitting climate modeling:
604 Demonstrations, prospects, and challenges. *Reviews of geophysics*, 53(2): 323-361.

605 Reinares Martínez, I., and J. Chaboureaud, 2018: Precipitation and Mesoscale Convective Systems: Explicit versus
606 Parameterized Convection over Northern Africa. *Mon. Wea. Rev.*, 146, 797–812, [https://doi.org/10.1175/MWR-D-](https://doi.org/10.1175/MWR-D-17-0202.1)
607 17-0202.1.

608 Rempel, M., F. Senf, and H. Deneke, 2017: Object-Based Metrics for Forecast Verification of Convective
609 Development with Geostationary Satellite Data. *Mon. Wea. Rev.*, 145, 3161–3178, [https://doi.org/10.1175/MWR-](https://doi.org/10.1175/MWR-D-16-0480.1)
610 D-16-0480.1.

611 Skamarock, W. C., J. B. Klemp, J. Dudhia, D. O. Gill, D. M. Barker, M. G. Duda, X. Huang, W. Wang, and J. G.
612 Powers (2008), A description of the advanced research WRF version 3, NCAR Tech. Note, NCAR/TN-475 + STR,
613 8 pp., Natl. Cent. for Atmos. Res., Boulder, Colo. [Available at <http://www.mmm.ucar.edu/wrf/users/docs/arw619>
614 v3.pdf, 2008.]

615 Sun, X., M. Xue, J. Brotzge, R. A. McPherson, X.-M. Hu, and X.-Q. Yang (2016), An evaluation of dynamical
616 downscaling of Central Plains summer precipitation using a WRF-based regional climate model at a convection-
617 permitting 4 km resolution, *J. Geophys. Res. Atmos.*, 121, 13,801–13,825, doi:10.1002/2016JD024796.

618 Tang, J. , Wang, S. , Niu, X. , Hui, P. , Zong, P. , & Wang, X. . (2017). Impact of spectral nudging on regional
619 climate simulation over cordex east asia using wrf. *Climate dynamics*, 48(7-8), 2339-2357.

620 von Storch H, Langenberg H, Feser F. A spectral nudging technique for dynamical downscaling purposes[J].
621 *Monthly weather review*, 2000, 128(10): 3664-3673.

622 Wang, J., X. Dong, A. Kennedy, B. Hagenhoff, and B. Xi, 2019: A Regime-Based Evaluation of Southern and
623 Northern Great Plains Warm-Season Precipitation Events in WRF. *Wea. Forecasting*, 34, 805–831,
624 <https://doi.org/10.1175/WAF-D-19-0025.1>.

625 Xiong, Z., and Yan, X. (2013), Building a high-resolution regional climate model for the Heihe River Basin and
626 simulating precipitation over this region. *Chinese science bulletin*, 58(36), 4670-4678.

627 Yun, Y. , Liu, C. , Luo, Y. , Liang, X. , Huang, L. , & Chen, F. , et al. (2020). Convection-permitting regional
628 climate simulation of warm-season precipitation over eastern china. *Climate Dynamics*, 54(3), 1469-1489.

629
630
631
632
633
634
635
636
637

638
639
640
641
642
643
644
645
646
647
648
649
650
651
652
653
654
655
656
657
658
659

660 **Table and Figure Captions**

661 **Table 1** Comparisons of the occurrence frequency of the trajectories in four directions from
662 CMORPH, CP NOSN and SN. Numbers in brackets represent the contribution (%) relative to the
663 total trajectories for CMORPH, CP NOSN, CP SN, respectively.

664 **Table 2** Comparisons of the properties of precipitation systems in CMORPH, CP NOSN and SN.
665 Numbers in brackets represent the differences (%) relative to CMORPH.

666 **Table 3.** The spatial COR RMSE of accumulated precipitation amount for systems with different
667 durations between CMORPH and CP NOSN and CP SN.

668 **Fig. 1** An example for identifying and tracking the precipitation systems occurred from 0200 UTC
669 to 0400 UTC 2 July 2006. Precipitation derived from CMORPH (a-c) and identified precipitation
670 systems represented by the same color at each time step (d-f).

671 **Fig. 2** Tracks of precipitation systems derived from CMORPH (a), CP NOSN (b) and CP SN (c) in
672 MJJASO 1998-2007. Colors of the tracks correspond to the systems' maximum rainfall. Track
673 density differences (d-e) between model and observation, which are binned to $0.5^{\circ} \times 0.5^{\circ}$ grid
674 spacing. The black solid lines outlined North China Plain (107° – 122° E, 32° – 41° N), Mei-yu
675 Region (112° – 122° E, 27° – 32° N), Southern China (110° – 120° E, 22° – 27° N), Sichuan Basin
676 (103° – 108° E, 28° – 32° N) and Yungui Plateau (102° – 110° E, 22° – 28° N), respectively.

677 **Fig. 3** Spatial distribution of the genesis density (a-c) and the moving speed (d-f) of precipitation

678 systems as identified and tracked from CMORPH, CP NOSN and CP SN in MJJASO 1998-2007.
 679 Note that the genesis density and moving speed are binned to $0.5^{\circ} \times 0.5^{\circ}$ grid spacing. The sub-
 680 regions are outlined by black lines as shown in Fig. 2.

681 **Fig. 4** Density-scatter plot of the object coverage area (a-c), intensity (d-f), eccentricity (h-j) and
 682 duration from CMORPH, CP NOSN and CP SN in MJJASO 1998-2007, the black dotted lines are
 683 represented by objects with duration of 48 hr.

684 **Fig. 5** The mean intensity and mean maximal rainfall as a function of coverage area for all
 685 systems (a, d), shorter-duration systems (b, e) and longer-duration systems (c, f) from CMORPH,
 686 CP NOSN and CP SN in MJJASO 1998-2007.

687 **Fig 6.** The spatial distribution of total precipitation amount for all systems (a-c), shorter-duration
 688 (d-f), longer-duration systems (g-i) detected from CMORPH, CP NOSN and CP SN in MJJASO
 689 1998-2007. The sub-regions are outlined by black lines as shown in Fig. 2.

690 **Fig 7.** Histograms of the occurrence frequency (a) of nine categories classified by different
 691 duration and their contributions (b) to total amount, and box-and-whisker plots of the average
 692 intensity (c) and coverage area (d) for nine categories from CMORPH, CP NOSN and CP SN in
 693 MJJASO 1998-2007.

694

695

696

697

698

699

700

701

702

703

704 **Table 1** Comparisons of the occurrence frequency of the trajectories in four directions from
 705 CMORPH, CP NOSN and SN. Numbers in brackets represent the contribution (%) relative to the
 706 total trajectories for CMORPH, CP NOSN, CP SN, respectively.

Movement Direction	Occurrence Frequency		
	CMORPH	CP NOSN	CP SN
Northeastward	21709 [31.8%]	11883 [32.1%]	12985[33.3%]
Northwestward	9466 [13.8%]	7485 [20.2%]	7172[18.4%]
Southwestward	17136[25.7%]	7914[21.4%]	8160[20.9%]
Southeastward	20063[29.3%]	9698[26.3%]	10651[27.4%]
Total trajectories	68374	36980	38968

707

708

709

710

711 **Table 2** Comparisons of the properties of precipitation systems in CMORPH, CP NOSN and SN.
 712 Numbers in brackets represent the differences (%) relative to CMORPH.

	CMORPH	CP NOSN	CP SN

61

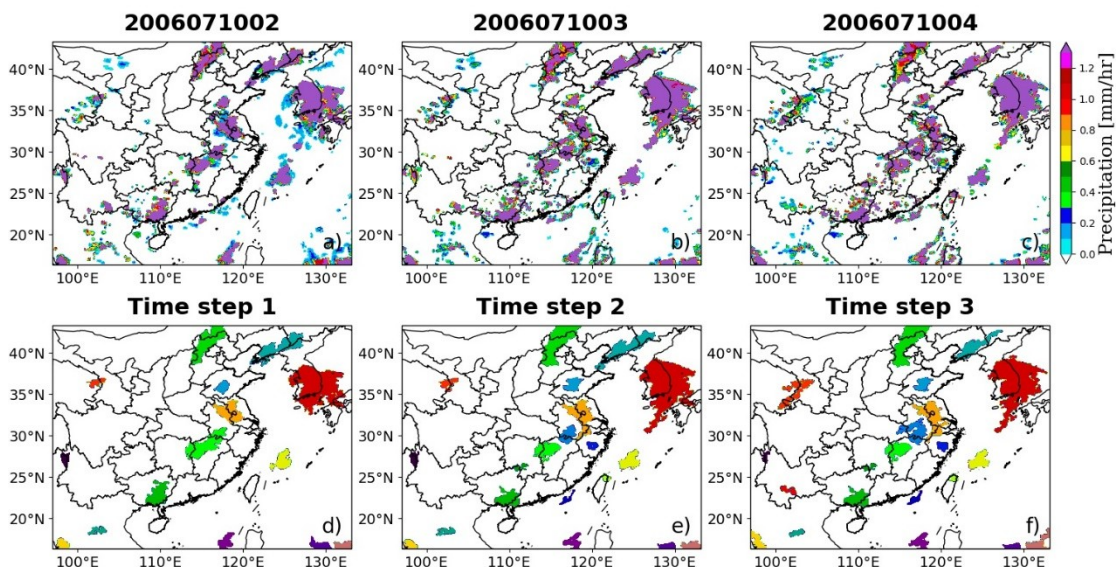
62

Average duration of systems (hr)	8.8	8.9 [+1.1%]	8.9 [+1.1%]
Average intensity of hourly rainfall (mm/hr)	1.8	3.2 [+77.8%]	3.2 [+77.8%]
Average coverage area of systems (km ²)	25986	23241 [-10.6%]	22314 [-14.0%]
Average eccentricity of systems	0.84	0.85 [+1.2%]	0.85 [+1.2%]

713
714
715
716
717
718
719

Table 3. The spatial COR RMSE of accumulated precipitation amount for systems with different durations between CMORPH and CP NOSN and CP SN.

Duration		CP NOSN		CP SN	
		COR	RMSE	COR	RMSE
3-6hr (Class A)		0.74	2.24	0.75	2.50
6-12hr (Class B)		0.76	3.23	0.76	3.23
12-24hr (Class C)		0.72	6.32	0.72	6.40
24-48hr (Class D)		0.43	7.62	0.48	7.61
Total	3-48hr	0.74	1.38	0.77	1.36
Total	>=48hr	0.68	17.3	0.78	12.8
48-72hr (Class E)		0.39	5.68	0.46	5.16
72-96hr (Class F)		0.31	4.65	0.55	3.50
96-120hr (Class G)		0.56	4.91	0.66	4.91
120-144hr (Class H)		0.68	3.71	0.81	2.08
>=144hr (Class I)		0.77	4.54	0.80	3.13
All		0.78	20.4	0.80	18.8



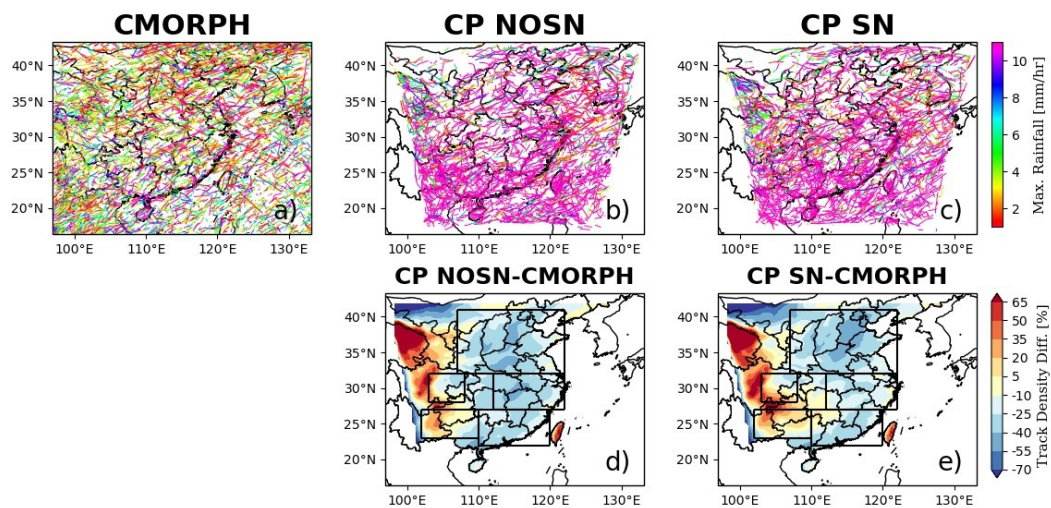
720
721

Fig. 1 An example for identifying and tracking the precipitation systems occurred from 0200 UTC

63
64

722 to 0400 UTC 2 July 2006. Precipitation derived from CMORPH (a-c) and identified precipitation
 723 systems represented by the same color at each time step (d-f).

724
 725
 726
 727
 728
 729
 730
 731
 732
 733
 734
 735
 736
 737
 738
 739
 740
 741
 742
 743
 744
 745
 746
 747



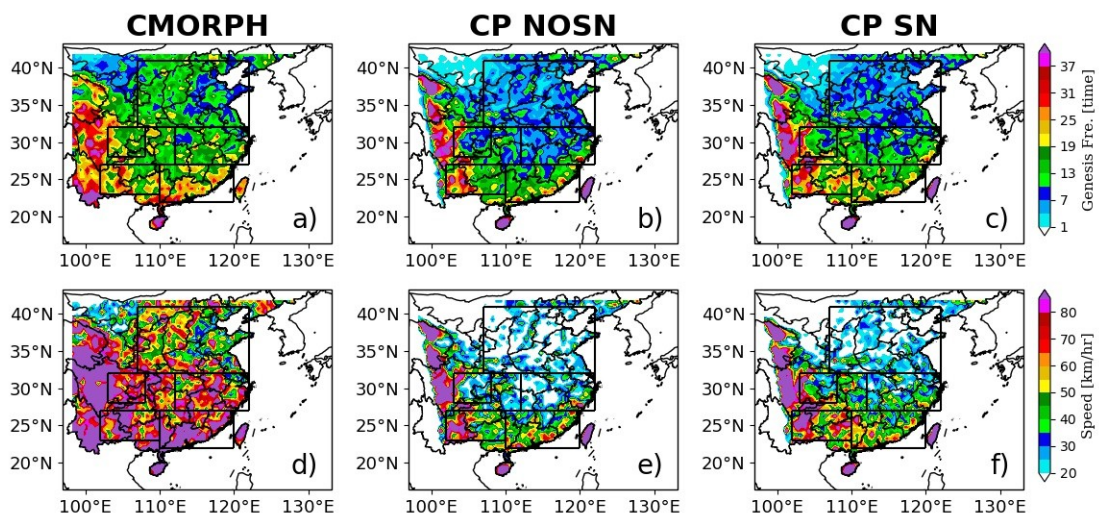
748

749 **Fig. 2** Tracks of precipitation systems derived from CMORPH (a), CP NOSN (b) and CP SN (c) in
 750 MJJASO 1998-2007. Colors of the tracks correspond to the systems' maximum rainfall. Track
 751 density differences (d-e) between model and observation, which are binned to $0.5^\circ \times 0.5^\circ$ grid
 752 spacing. The black solid lines outlined North China Plain ($107^\circ\text{--}122^\circ$ E, $32^\circ\text{--}41^\circ$ N), Mei-yu
 753 Region ($112^\circ\text{--}122^\circ$ E, $27^\circ\text{--}32^\circ$ N), Southern China ($110^\circ\text{--}120^\circ$ E, $22^\circ\text{--}27^\circ$ N), Sichuan Basin

65
 66

754 (103°–108° E, 28°– 32° N) and Yungui Plateau (102°–110° E, 22°– 28° N), respectively.

755
756
757
758
759
760
761
762
763
764
765
766
767
768
769
770
771
772
773
774
775
776
777
778
779

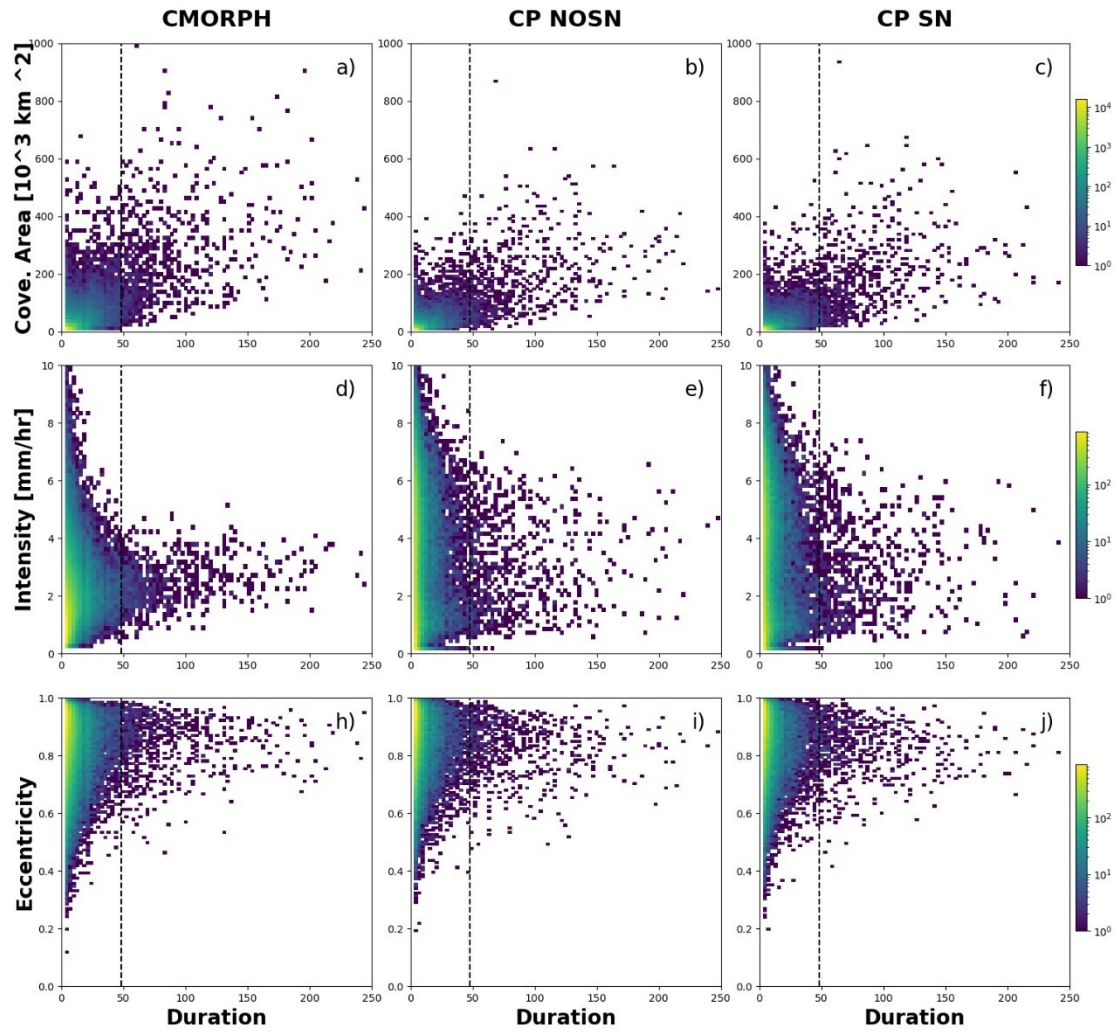


780
781
782
783
784
785

Fig. 3 Spatial distribution of the genesis density (a-c) and the moving speed (d-f) of precipitation systems as identified and tracked from CMORPH, CP NOSN and CP SN in MJJASO 1998-2007. Note that the genesis density and moving speed are binned to $0.5^\circ \times 0.5^\circ$ grid spacing. The sub-regions are outlined by black lines as shown in Fig. 2.

67
68

786
787
788
789
790
791
792
793
794
795
796
797
798
799
800
801
802
803
804
805
806
807
808
809
810
811



812

813 **Fig. 4** Density-scatter plot of the object coverage area (a-c), intensity (d-f), eccentricity (h-j) and
 814 duration from CMORPH, CP NOSN and CP SN in MJJASO 1998-2007, the black dotted lines are
 815 represented by objects with duration of 48 hr.

816

817

818

819

820

821

822

823

824

825

826

827

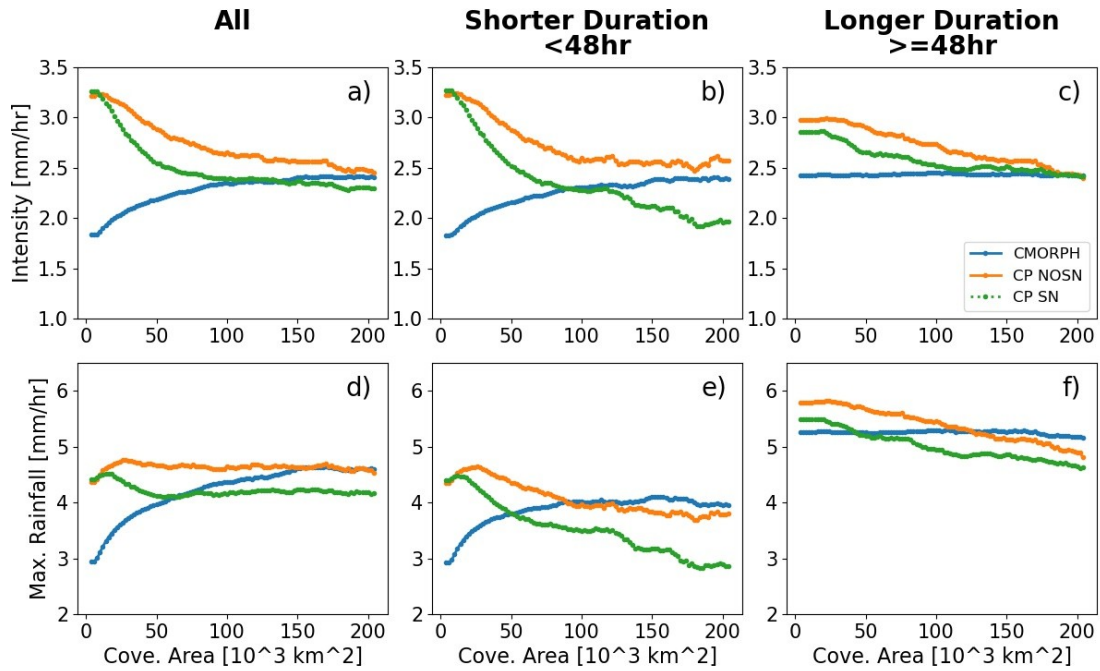
828

829

830

71

72



831

832 **Fig. 5** The mean intensity and mean maximal rainfall as a function of coverage area for all
 833 systems (a, d), shorter-duration systems (b, e) and longer-duration systems (c, f) from CMORPH,
 834 CP NOSN and CP SN in MJJASO 1998-2007.

835

836

837

838

839

840

841

842

843

844

845

846

847

848

849

850

851

852

853

854

855

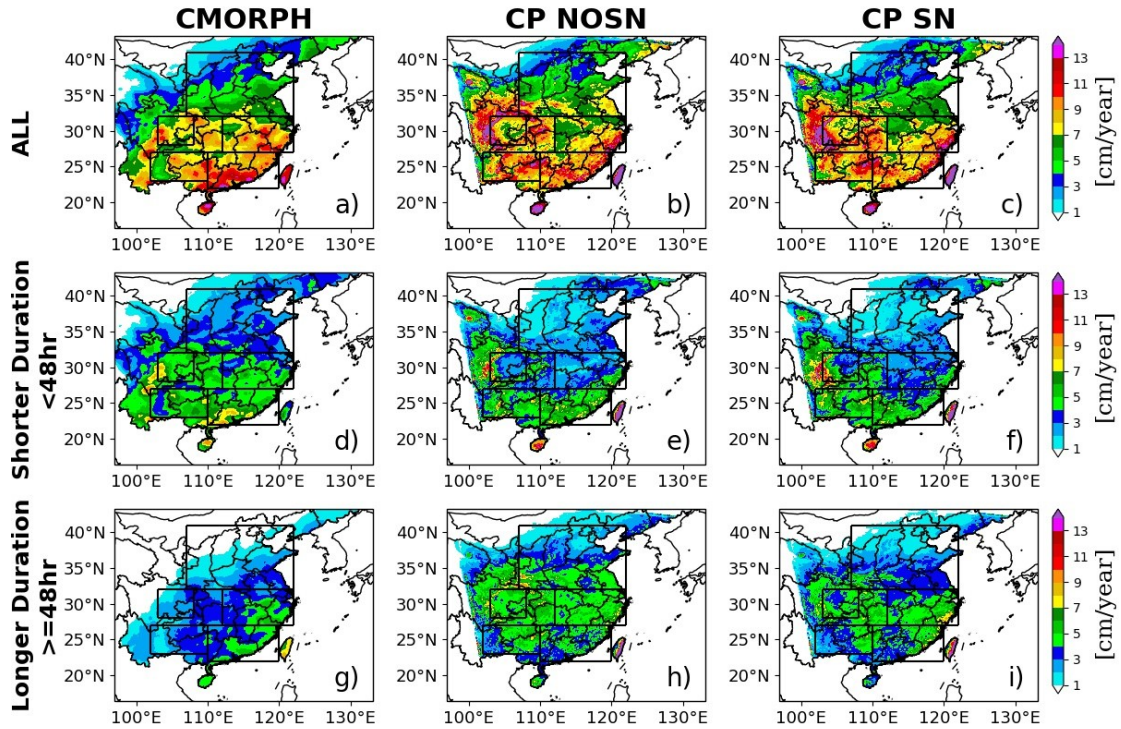
856

857

858

73

74



859

860 **Fig 6.** The spatial distribution of total precipitation amount for all systems (a-c), shorter-duration
 861 (d-f), longer-duration systems (g-i) detected from CMORPH, CP NOSN and CP SN in MJJASO
 862 1998-2007. The sub-regions are outlined by black lines as shown in Fig. 2.

863

864

865

866

867

868

869

870

871

872

873

874

875

876

877

878

879

880

881

882

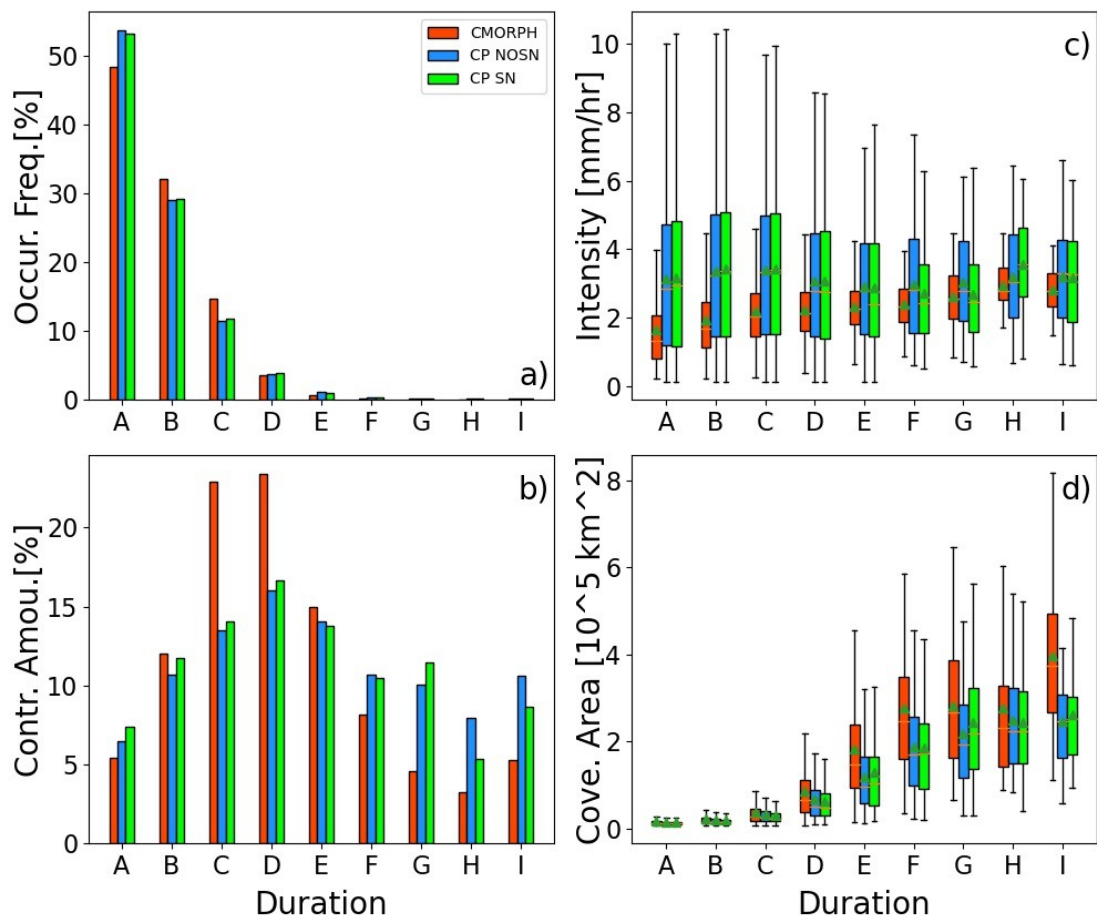
883

884

885

75

76



886

887 **Fig 7.** Histograms of the occurrence frequency (a) of nine categories classified by different
 888 duration and their contributions (b) to total amount, and box-and-whisker plots of the average
 889 intensity (c) and coverage area (d) for nine categories from CMORPH, CP NOSN and CP SN in
 890 MJJASO 1998-2007.